





Hierarchical micro/nanostructured silver hollow fiber boosts electroreduction of carbon dioxide

Shoujie Li^{1,2,3}, Wei Chen^{1,2} , Xiao Dong¹ , Chang Zhu^{1,2}, Aohui Chen^{1,2,3}, Yanfang Song^{1,2}, Guihua Li^{1,2}, Wei Wei^{1,2,3}  & Yuhan Sun^{1,2,3} 

Efficient conversion of CO₂ to commodity chemicals by sustainable way is of great significance for achieving carbon neutrality. Although considerable progress has been made in CO₂ utilization, highly efficient CO₂ conversion with high space velocity under mild conditions remains a challenge. Here, we report a hierarchical micro/nanostructured silver hollow fiber electrode that reduces CO₂ to CO with a faradaic efficiency of 93% and a current density of 1.26 A · cm⁻² at a potential of -0.83 V vs. RHE. Exceeding 50% conversions of as high as 31,000 mL · g_{cat}⁻¹ · h⁻¹ CO₂ are achieved at ambient temperature and pressure. Electrochemical results and time-resolved operando Raman spectra demonstrate that enhanced three-phase interface reactions and oriented mass transfers synergistically boost CO production.

¹Low-Carbon Conversion Science and Engineering Center, Shanghai Advanced Research Institute, Chinese Academy of Sciences, Shanghai 201210, PR China. ²University of Chinese Academy of Sciences, Beijing 100049, PR China. ³School of Physical Science and Technology, ShanghaiTech University, Shanghai 201203, PR China. ✉email: chenw@sari.ac.cn; weiwei@sari.ac.cn; sunyh@sari.ac.cn

Large-scale CO₂ utilization, abating carbon emissions while producing commodity chemicals, is a promising strategy for achieving carbon neutrality^{1–3}. Thermocatalytic routes such as CO₂ hydrogenation to methanol or other compounds exhibit industrial potential but suffering from the dilemmas of hydrogen sources and severe reaction conditions^{4–6}. Recently, electrocatalytic CO₂ conversion has emerged as a remarkable technology that benefits from the desirable coupling of renewable electricity transition and CO₂ utilization^{7–10}. However, the efficiency of CO₂ electroreduction is much inferior to thermocatalytic CO₂ conversion processes due to the limited CO₂ solubility in electrolyte solutions and divergent kinetics^{9,11}. One tactic for addressing these issues is adopting gas-diffusion electrodes that consist of highly active catalysts decorated with superhydrophobic polytetrafluoroethylene and conductive carbon layers^{12–15}. Regarding such gas-diffusion electrodes, these multiple components are assembled via subtle procedures to build complicated configurations, which could hinder their practical scale-up. Although large current densities and high faradaic efficiencies of various products have been realized over these gas-diffusion electrodes^{12,16}, their CO₂ conversion rates especially at high flow rates are still lower than 20% (Supplementary Table 1). Furthermore, three-dimensional hollow fiber electrodes with a compact structure exhibit promising potentials in efficient and high-rate CO₂ electroreduction by virtue of improved mass transport^{17–21}. To date, the hollow fiber electrodes still deliver too limited current densities ($\leq 200 \text{ mA} \cdot \text{cm}^{-2}$) to afford an economically viable CO₂ electrochemical conversion^{19,20}.

Herein, we report a hollow fiber electrode with hierarchical micro/nanostructures composed of only metallic silver (Ag) for electroreducing CO₂ to CO. Such a porous hollow-fiber Ag electrode acting as a CO₂ disperser can not only enhance three-phase interface reactions but also guide mass transfers during electrolysis (Fig. 1). As a result, CO₂ conversions exceed 50% at a high space velocity of $31,000 \text{ mL} \cdot \text{g}_{\text{cat}}^{-1} \cdot \text{h}^{-1}$ corresponding to a flow rate of $60 \text{ mL} \cdot \text{min}^{-1}$ under ambient conditions, maintaining stable large current densities ($\sim 1.26 \text{ A} \cdot \text{cm}^{-2}$) and high CO faradaic efficiencies ($\sim 93\%$) in a continuous test for a long lifespan, and this represents an encouraging headway in sustainable CO₂ utilization.

Results and discussion

Structure and composition. The silver hollow fiber (Ag HF) was first fabricated by a combined phase-inversion/sintering process from commercial Ag powder (Supplementary Fig. 1), followed by electrochemical redox activation treatments to obtain an activated Ag HF (Supplementary Figs. 2–4). The fused silver particles from

the outer surface of Ag HF rather than spherical ones in pristine Ag powder (Supplementary Figs. 5, 6) implied that a well-integrated substrate was formed by sintering during Ag HF fabrication.

The surfaces of the slender Ag HF tubes exhibited metallic luster (Fig. 2a), and their scanning electron microscopy (SEM) images showed abundant micrometer-sized pores on the outer/inner surfaces and interconnected pores inside the wall of Ag HF (Fig. 2b, c and Supplementary Figs. 5b, 7a). By the electrochemical activation treatments to reconstruct the outer surface of Ag HF, partly ordered nanorods gathered at the outer region, configuring hierarchical micro/nanostructures in activated Ag HF (Fig. 2d, e and Supplementary Fig. 7b). The effective porosities of Ag HF and activated Ag HF, as determined by gas permeation tests, were 38% and 32%, respectively (Supplementary Fig. 8 and Fig. 2f). Both X-ray diffraction (XRD) (Fig. 2g) and X-ray photoelectron spectroscopy (XPS) (Fig. 2h) verified that the bulk and surface compositions of Ag HF and activated Ag HF were identical with metallic silver (Supplementary Figs. 9, 10).

Electrocatalytic performance. The Ag HF array comprising ten tubes was used as the working electrode (Supplementary Fig. 11) and subjected to the potentiostatic electrolysis of CO₂ after the electrochemical activation treatments. Over a single tube of the activated Ag HF electrode, CO₂ molecules were highly dispersed via penetrating through the porous wall of activated Ag HF, and CO was produced at the gas-liquid-solid three-phase interface sites (Fig. 1). The CO partial current density (j_{CO}), i.e., the total current density \times CO faradaic efficiency, showed superior in the relatively concentrated solutions with the best performance in 1.5 M KHCO₃ (Supplementary Fig. 12). On basis of the intrinsic structure characteristics of activated Ag HF, the CO₂ flow rate was fixed at $60 \text{ mL} \cdot \text{min}^{-1}$ during CO₂ electroreduction to obtain the optimal electrocatalytic performance (Supplementary Fig. 13).

As shown in Fig. 3a, only CO and H₂ were detected over the activated Ag HF electrode (Supplementary Fig. 14) with their faradaic efficiency sum almost equaling 100% in the potential range of -0.35 to -0.89 V . The H₂ faradaic efficiency was always less than 3% up till -0.72 V while the total current density kept growing rapidly. At -0.83 V , the CO faradaic efficiency was 93% with the total current density of $1.26 \text{ A} \cdot \text{cm}^{-2}$. Then, the CO faradaic efficiency dropped down to 83% at -0.89 V , although the total current density increased to $1.69 \text{ A} \cdot \text{cm}^{-2}$, implying a rising hydrogen evolution reaction (HER) at more negative potentials. Further evaluation of the durability of the activated Ag HF electrode was performed in a continuous CO₂ electrolysis test operated at -0.83 V . The CO faradaic efficiency remained

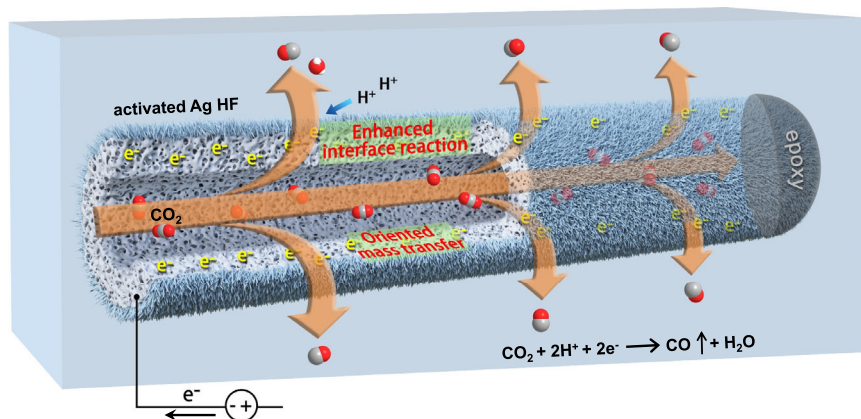


Fig. 1 Function outline of hollow-fiber silver electrode. Schematic illustration of hierarchical micro/nanostructured silver hollow fiber for boosting CO₂ electroreduction to CO.

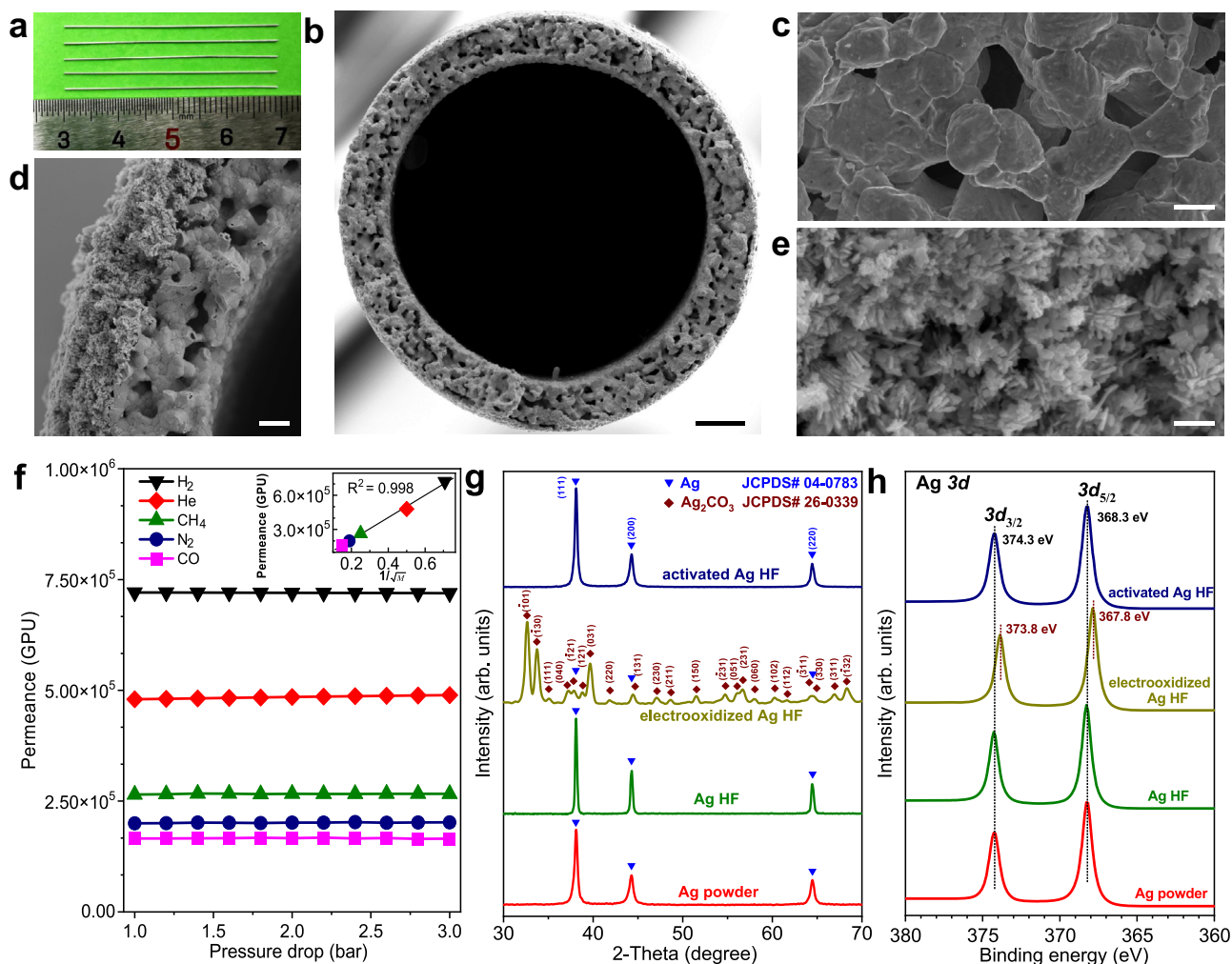


Fig. 2 Structural and compositional characterization. **a** Optical image of the as-fabricated Ag HF tubes. SEM images of **b, d**, cross sections and **c, e**, outer surfaces of **b, c**, Ag HF and **d, e**, activated Ag HF. Scale bars in **b, c, d** and **e** are 50 μm , 5 μm , 10 μm and 500 nm, respectively. **f** Gas permeances of activated Ag HF. GPU denotes gas permeation unit. Inset: the permeances (at 1.0 bar) are proportional to the inverse square root of gas molecular weight. **g** XRD patterns, and **h**, XPS spectra of Ag HF and activated Ag HF.

between 93 and 92% and the total current density fluctuated between 1.26 and 1.24 $\text{A} \cdot \text{cm}^{-2}$, manifesting no declining sign for 170 h (Fig. 3b). The postreaction XRD (Supplementary Fig. 9) and XPS (Supplementary Fig. 10) revealed the unchanged compositions of activated Ag HF after the electrolysis, and the corresponding structural features were also highly similar to those before the electrolysis (Supplementary Fig. 8), which were responsible for the stable CO_2 electroreduction performance.

CO_2 conversion rate is an important common criterion for both thermocatalytic and electrocatalytic processes, and their overall comparisons are displayed in Fig. 3c. In the current density range from 2 to 400 $\text{mA} \cdot \text{cm}^{-2}$, the CO_2 conversion rates of activated Ag HF were comparable to those over other prominent catalysts reported in electrocatalysis. Note that the CO_2 conversion rates further increased rapidly with negative-shifting potentials (Supplementary Fig. 15) and increasing current densities, which approached the theoretical predictions, far outperforming the previously reported electrocatalysts (Fig. 3c and Supplementary Table 1). At -0.83 V, the CO_2 conversion rate of activated Ag HF was 54% with sustained performance during the long-term test (Fig. 3b). Furthermore, the thermocatalytic catalysts run at high temperature (170–360 $^\circ\text{C}$) and pressure (1–5 MPa) delivered relatively low CO_2 conversion rates (less than 22%) at high space velocities ($\geq 18,000 \text{ mL} \cdot \text{g}_{\text{cat}}^{-1} \cdot \text{h}^{-1}$)

(Fig. 3c and Supplementary Table 1). In contrast, the CO_2 conversion rates over the activated Ag HF electrode at CO_2 space velocity of 31,000 $\text{mL} \cdot \text{g}_{\text{cat}}^{-1} \cdot \text{h}^{-1}$ exceeded 28% just from -0.72 V and 54% from -0.83 V under ambient conditions, even higher than those over low-space-velocity-run catalysts of CO_2 hydrogenation (Supplementary Fig. 15 and Supplementary Table 1).

Previous studies^{22–25} reported Ag electrocatalysts possessing the capability to selectively reduce CO_2 to CO, but their current densities of long-term tests remained below 200 $\text{mA} \cdot \text{cm}^{-2}$ (Supplementary Table 1), far from the $\geq 400 \text{ mA} \cdot \text{cm}^{-2}$ regime for industrial applications^{26,27}. In sharp contrast, our activated Ag HF electrode manifested the sustained large current density ($\sim 1.26 \text{ A} \cdot \text{cm}^{-2}$) with high CO faradaic efficiency ($\sim 93\%$), implying a striking promotion in the intrinsic activity of Ag.

Electrochemical characterization. The electrochemically active surface areas (ECSAs) of activated Ag HF, Ag HF, activated Ag foil and Ag foil were determined by measuring their double-layer capacitance (C_{dl}) values via their cyclic voltammograms (Supplementary Fig. 16). Although the ECSA of activated Ag HF was only nearly 3 times that of activated Ag foil (Fig. 4a), the j_{CO} of activated Ag HF with the lower overpotential was almost two orders of magnitude larger than that of activated Ag foil (Fig. 4b

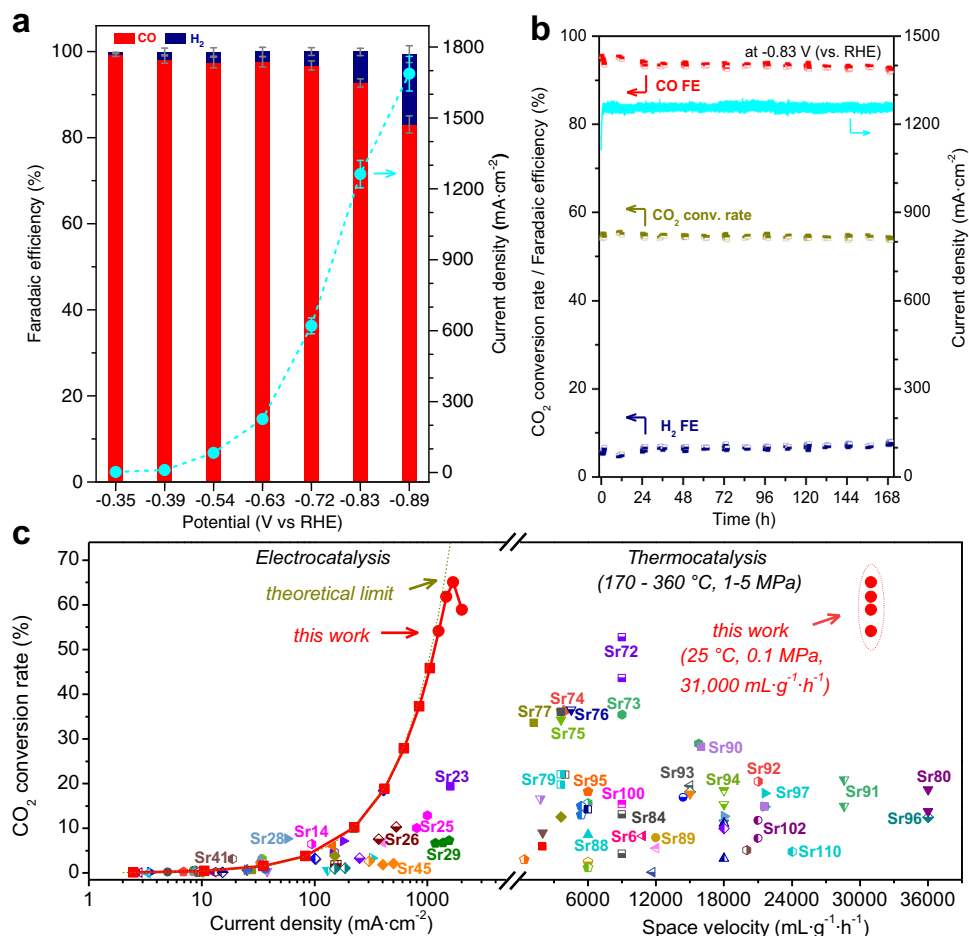


Fig. 3 Performance of activated Ag HF. **a** CO and H₂ faradaic efficiencies, and total current densities in the potential range of -0.35 to -0.89 V. Error bars in **a** were obtained from the average of six individual tests. **b** Long-term performance at -0.83 V. **c** CO₂ conversion rates with a space velocity of $31,000 \text{ mL} \cdot \text{g}_{\text{cat}}^{-1} \cdot \text{h}^{-1}$ at different current densities, and their overall comparison with other electrocatalytic and thermocatalytic CO₂ conversions. All comparison data points in **c** are from the references summarized in Supplementary Table S1, and the key data points are referred to the corresponding Supplementary references Sr_x, where *x* represents the reference number in Supplementary Information. CO₂-saturated 1.5 M KHCO₃ as the electrolyte solution, and the CO₂ flow rate of $60 \text{ mL} \cdot \text{min}^{-1}$.

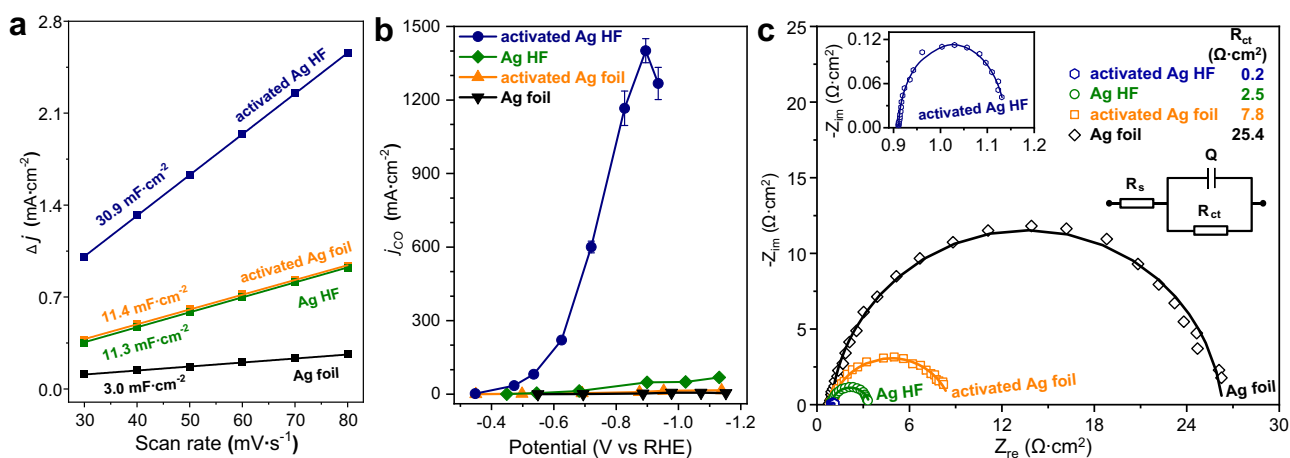


Fig. 4 Electrochemical characterization. **a** Plot of Δj (the difference of cathodic and anodic current densities, $j_c - j_a$) against the scan rates from cyclic voltammograms (Supplementary Fig. 16). **b** CO partial current density comparison, and error bars were obtained from the average of six individual tests. **c** EIS Nyquist plots of activated Ag HF, Ag HF, activated Ag foil and Ag foil. The inset in **c** shows the equivalent circuit.

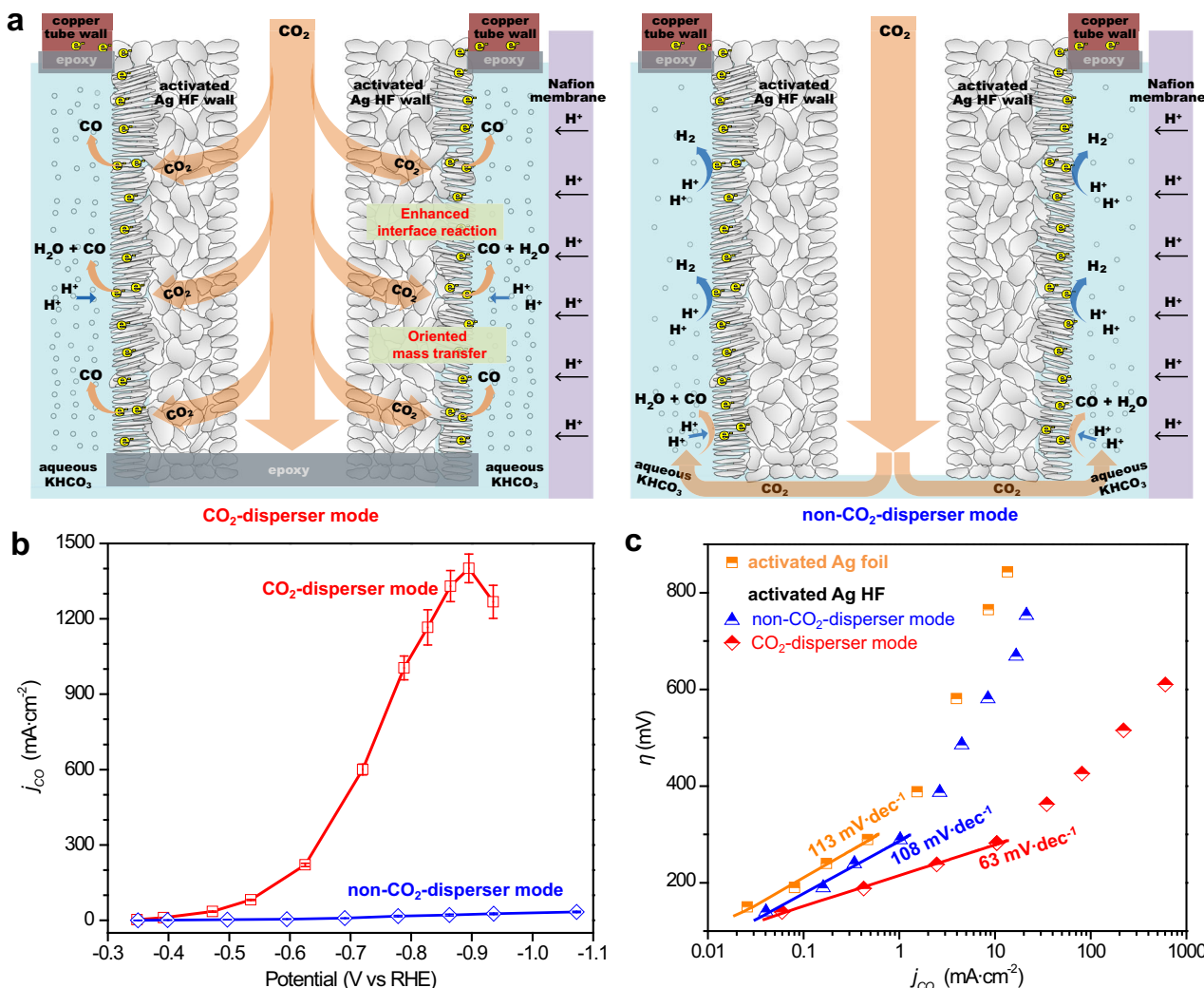


Fig. 5 CO₂ dispersion effect studies. **a** Schematic illustrations showing the processes of CO₂ electroreduction over activated Ag HF with the CO₂-disperser mode and the non-CO₂-disperser mode, respectively, and **b**, their CO partial current densities. Error bars in **b** were obtained from the average of six individual tests. **c** Tafel slopes of activated Ag foil and activated Ag HF with different dispersion modes.

and Supplementary Fig. 17). This implied that the high ECSA only played a secondary role in efficiently producing CO over activated Ag HF.

Furthermore, the electrochemical impedance spectroscopy (EIS) measurements were performed to study the electron transfer behaviors of the activated Ag HF, Ag HF, activated Ag foil and Ag foil electrodes, and their impedance spectra in the complex plane (Nyquist plot) are presented in Fig. 4c. The activated Ag HF electrode exhibited the smallest R_{ct} ($0.2 \Omega \cdot \text{cm}^2$) compared with those of Ag HF ($2.5 \Omega \cdot \text{cm}^2$), activated Ag foil ($7.8 \Omega \cdot \text{cm}^2$) and Ag foil ($25.4 \Omega \cdot \text{cm}^2$), indicating the most favorable CO₂ reduction kinetics over activated Ag HF.

CO₂ dispersion effects. In comparison with other counterparts, activated Ag HF was distinguished in that it possessed the unique CO₂ diffusion manner acting as a CO₂ disperser. That is the restrained environment of activated Ag HF offered a scenario that CO₂ were compulsively interacted with active sites when penetrating through the porous wall (Fig. 5a), resulting in enhanced three-phase interface reactions and optimized kinetics to produce CO efficiently. Obviously, such CO₂ dispersion effects of activated Ag HF vanished just switching to non-CO₂-disperser mode (Fig. 5a, b). The comparison of CO partial current densities over

the activated Ag HF electrode with the CO₂-disperser and non-CO₂-disperser modes is shown in Fig. 5b. As the potential negatively shifted from -0.35 to -0.94 V, the j_{CO} of activated Ag HF using the CO₂-disperser mode increased quickly and reached the maximum value of $1402 \text{ mA} \cdot \text{cm}^{-2}$ at -0.89 V, then slightly decreased to $1268 \text{ mA} \cdot \text{cm}^{-2}$ at -0.94 V. In sharp contrast, activated Ag HF using the non-CO₂-disperser mode always delivered rather low j_{CO} values and showed a maximum value of only $33 \text{ mA} \cdot \text{cm}^{-2}$ at -1.07 V. These results indicated that the CO₂-disperser mode was uniquely superior to the non-CO₂-disperser mode.

It is generally known that large current densities in water-based electrolytes will lead to the high local pH near the electrode surface, which inhibits the HER and increases CO₂ reduction due to the proton depletion^{28–30}. Besides such CO₂ reduction promotion from local pH variation, our activated Ag HF electrode could deliver large and stable current density lying in the enhanced three-phase interface reactions and mass transfers. That is the high-flow-rate CO₂ rushing out from the porous hollow fiber wall to react on the abundant active Ag nanorods at the outer region, thereby maintaining extremely high local CO₂ concentration at three-phase interface sites for significant CO₂ electroreduction rather than HER^{31,32}. Consequently, such a

hollow fiber dispersion design maximizes the efficiency of the three-phase reaction interfaces, showing a promising potential compared with the conventional membrane electrode assembly.

Furthermore, a comparison of the kinetic data extracted from the Tafel plots, namely, the overpotential (η) versus $\log(j_{\text{CO}})$, was made for activated Ag foil and activated Ag HF with the non-CO₂-dispenser and CO₂-dispenser modes, as shown in Fig. 5c. In the low overpotential regime (i.e., Tafel linearity) of -140 to -290 mV, a Tafel slope of $113 \text{ mV} \cdot \text{dec}^{-1}$ was obtained for activated Ag foil, close to the value of $118 \text{ mV} \cdot \text{dec}^{-1}$ expected for a rate-determining single-electron transfer at the electrode surface³³. This result indicated that the initial one-electron transfer for CO₂ activation over activated Ag foil to form an adsorbed *COO⁻ intermediate (Supplementary Fig. 18) was the rate-determining step, in consistency with previous reports^{33,34}. Furthermore, a dramatically increased Tafel slope for activated Ag foil was observed at relatively high overpotentials, implying that CO₂ electroreduction likely reached a mass transfer limitation^{34,35}. In contrast, activated Ag HF with the CO₂-dispenser mode showed the smallest Tafel slope ($63 \text{ mV} \cdot \text{dec}^{-1}$), close to the theoretical value of $59 \text{ mV} \cdot \text{dec}^{-1}$ ^{35,36}, suggesting a fast initial one-electron transfer step to form *COO⁻ and a subsequent slower chemical reaction as the rate-determining step (Supplementary Fig. 18). The Tafel slope of activated Ag HF with the CO₂-dispenser mode at high overpotential regime was also much smaller than that of activated Ag foil, implying the favorable mass transfer. Interestingly, the Tafel slope for activated Ag HF with the non-CO₂-dispenser was $108 \text{ mV} \cdot \text{dec}^{-1}$, which was close to the value of $113 \text{ mV} \cdot \text{dec}^{-1}$ for activated Ag foil. This result indicated that both had the same rate-determining step, namely, the initial one-electron transfer, which also confirmed the superiority of the CO₂-dispenser mode for CO₂ reduction. In addition, the high-overpotential Tafel slope for activated Ag HF with the non-CO₂-dispenser mode was closer to that for activated Ag foil. These results indicated that the improved initial one-electron transfer and mass transfer jointly enhanced the intrinsic CO₂ reduction activity of activated Ag HF with the CO₂-dispenser mode, resulting in high selectivity and activity for the electrocatalytic reduction of CO₂ to CO.

Mechanistic studies. Isotope-labelling experiments were conducted using C¹⁸O₂ and D₂O as feedstocks to reveal the mass migrations involved in CO₂ electroreduction over activated Ag HF. The results in Fig. 6a and Supplementary Fig. 19 suggested that CO production was derived from the CO₂ dissociation to form one O atom, which coupled with two protons (H⁺) to generate H₂O (Fig. 5a), while anodic water oxidation released and supplied protons to participate in cathodic CO₂ reduction. This indicated that the product CO originated from the reduction of CO₂ and the anodic reaction maintained the proton and charge balances of the overall CO₂ electroreduction reaction.

Time-resolved operando Raman spectroscopy was resorted to further reveal the formation and evolution of key intermediates during CO₂ electroreduction. The typical operando Raman spectra of both activated Ag HF and activated Ag foil (Supplementary Fig. 20) showed two Raman bands at 532 and 390–410 cm⁻¹, corresponding to adsorbed *COO⁻ and *COOH intermediates, respectively^{37,38}, besides bicarbonate ion related peaks above 1000 cm⁻¹^{39–41}. The chronological appearances of *COO⁻ and *COOH (Fig. 6b and Supplementary Fig. 21c) implied the step-by-step reduction of CO₂, i.e., the initial step to form *COO⁻ and the second step to form *COOH, in agreement with the proposed mechanism (Supplementary Fig. 18).

After power-on for 720 ms (**t1**), *COO⁻ Raman peak over activated Ag HF appeared, and then its intensity increased quickly and reached the maximum at 2720 ms (**t2**) (Fig. 6b and d). Regarding activated Ag foil, the *COO⁻ peak appeared at

660 ms (**t1'**), and the peak intensity reached a maximum at 3080 ms (**t2'**) (Supplementary Fig. 21c and Fig. 6d). Compared to activated Ag foil, more *COO⁻ intermediates were formed and adsorbed over activated Ag HF in a shorter time (Fig. 6d and Supplementary Figs. 21a, c), implying the superior capability of CO₂ activation over activated Ag HF, which probably profited from the reduced CO₂ diffusion distance in the CO₂-dispenser mode.

Subsequently, we investigated the variation of adsorbed *COO⁻ over activated Ag HF and activated Ag foil during the power-off stages (Fig. 6c and Supplementary Fig. 21d). As soon as the power was off, the 532 cm⁻¹ $\nu_{\text{*COO}^-}$ redshifted abruptly for both electrodes due to the Stark effect^{41–44}, indicating the distinct impact of electric field on the adsorption of intermediates (Supplementary Fig. 22). The *COO⁻ peak vanished over activated Ag HF after power-off for 1050 s (**t3**) (Fig. 6c, d), whereas over activated Ag foil after power-off for 1400 s (**t3'**) (Supplementary Fig. 21d and Fig. 6d). Moreover, the dissipation time of *COO⁻ over activated Ag HF with non-CO₂-dispenser mode was 1380 s (**t3''**) (Supplementary Fig. 23), which was close to that (1400 s, **t3'**) over activated Ag foil. The faster dissipation of adsorbed *COO⁻ benefited from the one-way CO₂ flow manner of activated Ag HF with the CO₂-dispenser mode (Fig. 6d). While direct Raman observations on the formation and desorption of *CO species were not available at present, to be explored in further study.

Consequently, these Raman results suggested that the oriented mass transfers induced by the CO₂-dispenser mode of activated Ag HF could not only favor the diffusion of CO₂ to active sites but also facilitate the desorption of adsorbed species from the electrode surface, resulting in the improved overall kinetics of CO₂ reduction.

Our results demonstrate that the electrocatalytic performance of CO₂ reduction could be greatly improved by adopting the micro/nanostructured hollow fiber configuration of silver, which provides new opportunities for heightening three-phase interface reactions and mass transfer kinetics simultaneously. In addition, the single composition and tough framework with simple fabrication procedures enable activated Ag HF to become an ideal industrial electrode with excellent durability. This work represents an encouraging headway in CO₂ electroreduction that may lead to scalable applications.

Methods

See the Supplementary Information for detailed description of the methods employed in this study.

Chemicals and materials. Ag powder (99.9%, 50 nm) was purchased from Ningbo Jinlei Nano Materials Co., Ltd. Ag foil (99.9%, 1 mm thick) was purchased from Shanghai Macklin Biochemical Technology Co., Ltd. Polyetherimide (PEI) was purchased from Saudi Basic Industries Corporation (SABIC). N-Methyl-2-pyrrolidone (NMP) and potassium bicarbonate (KHCO₃) were purchased from Sinopharm Chemical Reagent Co., Ltd. Nafion 117 proton exchange membranes (PEM) with an average thickness of 183 μm were purchased from DuPont. 3-Trimethylsilyl-1-propane sulfonic acid sodium salt (DSS) was purchased from Sigma-Aldrich. Isotope-labeled C¹⁸O₂ (purity: 97 at.%) was purchased from Sigma-Aldrich. Deuterium oxide (D₂O) was purchased from Sigma-Aldrich. All chemicals were used as received without further purification. Electrolyte solutions were prepared using 18.2 M Ω H₂O (ultrapure water, from Master-S30UVF water purification system).

Catalyst preparation. Ag HF was first fabricated by a combined phase-inversion/sintering process, and then was treated by electrochemical redox activation to obtain activated Ag HF. More details can be found in Supplementary Preparations section as well as Supplementary Figs. 1 and 2.

Physical characterization. The cross-section and surface morphologies were observed by scanning electron microscopy (SEM) with a SUPRRATM 55 microscope using an accelerating voltage of 5.0 kV. Transmission electron microscopy

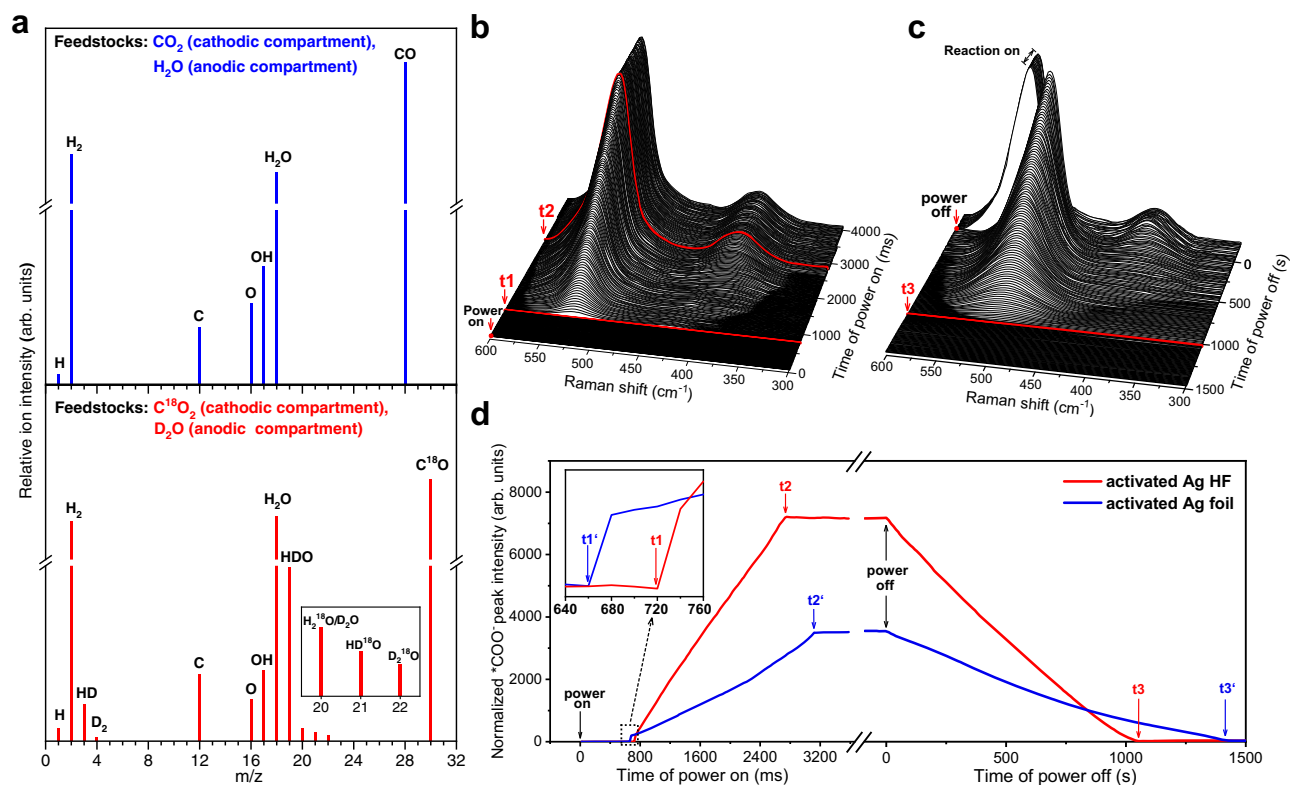


Fig. 6 Isotopic trace and time-resolved operando Raman results. **a** Mass spectrometric detections of the cathodic products over activated Ag HF using unlabeled feedstocks (upper) and isotopically labeled $C^{18}O_2$ and D_2O feedstocks (lower), respectively. **b, c** Time-resolved operando Raman spectra showing the formation, evolution and dissipation of intermediates over activated Ag HF. **d** Comparison of the normalized $*COO^-$ peak intensities of activated Ag HF and activated Ag foil during the power-on and power-off stages.

(TEM) investigations were conducted with a JEM-ARM300F microscope operated at 300 kV. X-ray diffraction (XRD) measurements were performed on a Rigaku Ultima 4 X-ray diffractometer using a $Cu K\alpha$ radiation source ($\lambda = 1.54056 \text{ \AA}$) at 40 kV and 40 mA. X-ray photoelectron spectroscopy (XPS) was conducted using a Quantum 2000 Scanning ESCA Microprobe instrument with a monochromatic Al $K\alpha$ source (1486.6 eV). The binding energies in all XPS spectra were calibrated according to the C 1s peak (284.8 eV).

Electrochemical characterization. Electrochemical characterization was performed on a Biologic VMP3 potentiostat in a gas-tight two-compartment electrolysis cell equipped with a KCl-saturated Ag/AgCl reference electrode and a platinum mesh (3 cm \times 3 cm) counter electrode. The electrochemically active surface area (ECSA) of the electrode was evaluated by the double-layer capacitance (C_{dl}). The C_{dl} was determined by performing cyclic voltammetry (CV) in the potential range of 0.4 to 0.5 V (vs. RHE) at different scan rates in CO_2 -saturated 1.5 M $KHCO_3$. The electrochemical impedance spectroscopy (EIS) measurements were performed in CO_2 -saturated 1.5 M $KHCO_3$ at -0.83 V (vs. RHE), and the frequency limits were typically set in the range of 0.1 Hz to 100 kHz with a voltage amplitude of 10 mV. Prior to the experiments, the electrolysis cell was vacuumized and then purged with CO_2 for 30 min, after which CO_2 was continuously delivered into the cathodic compartment at a constant rate of $10 \text{ mL} \cdot \text{min}^{-1}$. All the applied potentials were recorded against the KCl-saturated Ag/AgCl reference electrode and then converted to those versus the reversible hydrogen electrode (RHE) with iR compensation by the following equation: $E(\text{vs. RHE}) = E(\text{vs. Ag/AgCl}) + 0.197V + 0.0591V \times pH + 0.85iR_s$, where $E(\text{vs. Ag/AgCl})$ is the applied potential, pH is the *pondus hydrogenii* value of the electrolyte solutions with different concentrations (Supplementary Table 2), i is the current density at each applied potential, and R_s is the solution resistance obtained by EIS measurements (Supplementary Table 2), and 85% iR compensation was applied to correct the potential manually. All applied potentials in the main text and Supplementary Information referred to the RHE unless otherwise stated.

CO_2 electroreduction tests. The potentiostatic electroreductions of CO_2 over all electrodes were performed at ambient temperature and pressure on the Biologic VMP3 potentiostat using the gas-tight electrolysis cell. The cathodic and anodic compartments were separated by a Nafion 117 membrane, and the electrolysis cell was equipped with a KCl-saturated Ag/AgCl reference electrode in the cathodic compartment and a platinum mesh counter electrode in the anodic compartment.

More details can be found in Supplementary CO_2 Electroreduction and Product Quantifications section as well as Supplementary Fig. 14.

Isotopic trace. The isotope-labelling experiments were conducted under the same electrolysis reaction conditions that used $C^{18}O_2$ and D_2O as feedstocks. The feedstocks were supplied into the cathodic and anodic compartments of the electrolysis cell according to the following four situations: (I) nonisotope-labeled CO_2 was fed to the cathodic compartment, and nonisotope-labeled H_2O was used as the solvent in the anodic compartment; (II) nonisotope-labeled CO_2 was fed to the cathodic compartment, and D-labeled D_2O was used as the solvent in the anodic compartment; (III) ^{18}O -labeled $C^{18}O_2$ was fed to the cathodic compartment, and nonisotope-labeled H_2O was used as the solvent in the anodic compartment; (IV) ^{18}O -labeled $C^{18}O_2$ was fed to the cathodic compartment, and D-labeled D_2O was used as the solvent in the anodic compartment. The gas-phase exhausts from the cathodic compartment were first vented into 10 M NaOH solution to absorb unreacted CO_2 , and then the residual gases were detected by mass spectrometry (MS, GSD320-OmniStar, Pfeiffer Vacuum Corp., Germany). The offline catholyte sampled after 30-min electrolysis was placed into a water bath of $80 \text{ }^\circ\text{C}$ and then introduced into the mass spectrometer by a CO_2 flow of $10 \text{ mL} \cdot \text{min}^{-1}$. The MS data were analyzed and identified using QUADERA Version 4.60 software.

Time-resolved operando Raman spectroscopy. Time-resolved operando Raman measurements were carried out on a Raman spectrometer (i-Raman Pro BWS475-532H, B&W Tek Corp.) using a 532 nm excitation laser with a laser power of 25 mW. The Raman shift was calibrated to 520 cm^{-1} using a Si wafer. Activated Ag HF and activated Ag foil were used as the working electrodes in the electrolysis cell for the operando Raman measurements, respectively. The electrolyte solution was CO_2 -saturated 1.5 M $KHCO_3$ and the CO_2 flow rate was kept at $60 \text{ mL} \cdot \text{min}^{-1}$ for all Raman measurements. In order to decrease the disturbance of bubbles, the focus points of all Raman tests were generally close to the bottom region of the hollow fiber electrodes, where the bubbles were relatively sparse (Supplementary Fig. 11d). Raman spectra at the stable states of CO_2 electroreduction over a wider range of 300 to 2000 cm^{-1} were also obtained for the purpose of identifying the peaks from adsorbed bicarbonate ions or other possible species (Supplementary Fig. 20). Operando Raman spectra were recorded continuously within a range of 300 to 600 cm^{-1} without any time intervals (Supplementary Fig. 21), and in the meantime the potentials of CO_2 electroreduction were fixed at -0.83 and -0.69 V for activated Ag HF and activated Ag foil, respectively, which corresponded to their

favorable electrocatalytic performance, i.e., $\sim 1.26 \text{ A} \cdot \text{cm}^{-2}$ for activated Ag HF and $12 \text{ mA} \cdot \text{cm}^{-2}$ for activated Ag foil. Each Raman curve was obtained using a commercially available data-processing program (BWSpec 4.11 software), which was further subjected to smoothing treatment using commercial Origin 9.2 software before assembly of the operando Raman spectra. In addition, frequent power-on and power-off switching was applied during CO_2 electroreduction, which was monitored by Raman spectra in a range of 300 to 600 cm^{-1} to confirm the reproducibility of the Stark effect in our tests (Supplementary Fig. 22).

Data availability

All data supporting the findings of the study within this paper and Supplementary Information are available in the Source data file. Source data are provided with this paper.

Received: 20 December 2021; Accepted: 9 May 2022;

Published online: 02 June 2022

References

- Chu, S. & Majumdar, A. Opportunities and challenges for a sustainable energy future. *Nature* **488**, 294–303 (2012).
- Mallapaty, S. How China could be carbon neutral by mid-century. *Nature* **586**, 482–483 (2020).
- Jordaan, S. M. & Wang, C. Electrocatalytic conversion of carbon dioxide for the Paris goals. *Nat. Catal.* **4**, 915–920 (2021).
- Graciani, J. et al. Highly active copper-ceria and copper-ceria-titania catalysts for methanol synthesis from CO_2 . *Science* **345**, 546–550 (2014).
- Gao, P. et al. Direct conversion of CO_2 into liquid fuels with high selectivity over a bifunctional catalyst. *Nat. Chem.* **9**, 1019–1024 (2017).
- Hu, J. et al. Sulfur vacancy-rich MoS_2 as a catalyst for the hydrogenation of CO_2 to methanol. *Nat. Catal.* **4**, 242–250 (2021).
- Rabinowitz, J. A. & Kanan, M. W. The future of low-temperature carbon dioxide electrolysis depends on solving one basic problem. *Nat. Commun.* **11**, 5231 (2020).
- Lin, S. et al. Covalent organic frameworks comprising cobalt porphyrins for catalytic CO_2 reduction in water. *Science* **349**, 1208–1213 (2015).
- Wu, Y., Jiang, Z., Lu, X., Liang, Y. & Wang, H. Domino electroreduction of CO_2 to methanol on a molecular catalyst. *Nature* **575**, 639–642 (2019).
- Li, F. et al. Molecular tuning of CO_2 -to-ethylene conversion. *Nature* **577**, 509–513 (2020).
- Liu, M. et al. Enhanced electrocatalytic CO_2 reduction via field-induced reagent concentration. *Nature* **537**, 382–386 (2016).
- Lv, J. J. et al. A highly porous copper electrocatalyst for carbon dioxide reduction. *Adv. Mater.* **30**, e1803111 (2018).
- Dinh, C.-T. et al. CO_2 electroreduction to ethylene via hydroxide-mediated copper catalysis at an abrupt interface. *Science* **360**, 783–787 (2018).
- Ma, W. et al. Electrocatalytic reduction of CO_2 to ethylene and ethanol through hydrogen-assisted C–C coupling over fluorine-modified copper. *Nat. Catal.* **3**, 478–487 (2020).
- Dinh, C.-T., García de Arquer, F. P., Sinton, D. & Sargent, E. H. High rate, selective, and stable electroreduction of CO_2 to CO in basic and neutral media. *ACS Energy Lett.* **3**, 2835–2840 (2018).
- García de Arquer, F. P. et al. CO_2 electrolysis to multicarbon products at activities greater than 1 A cm^{-2} . *Science* **367**, 661–666 (2020).
- Kas, R. et al. Three-dimensional porous hollow fibre copper electrodes for efficient and high-rate electrochemical carbon dioxide reduction. *Nat. Commun.* **7**, 10748 (2016).
- Zhu, C. et al. Copper hollow fibre electrode for efficient CO_2 electroreduction. *J. Power Sources* **495**, 229814 (2021).
- Rabiee, H. et al. Tuning the product selectivity of the Cu hollow Fiber gas diffusion electrode for efficient CO_2 reduction to formate by controlled surface Sn electrodeposition. *ACS Appl. Mater. Interfaces* **12**, 21670–21681 (2020).
- Hummadi, K. K., Sustronk, A., Kas, R., Benes, N. & Mul, G. Optimizing temperature treatment of copper hollow fibers for the electrochemical reduction of CO_2 to CO. *Catalysts* **11**, 571 (2021).
- Bell, D. et al. Tubular hollow fibre electrodes for CO_2 reduction made from copper aluminum alloy with drastically increased intrinsic porosity. *Electrochem. Commun.* **111**, 106645 (2020).
- Lu, Q. et al. A selective and efficient electrocatalyst for carbon dioxide reduction. *Nat. Commun.* **5**, 3242 (2014).
- Ma, M., Trześniewski, B. J., Xie, J. & Smith, W. A. Selective and efficient reduction of carbon dioxide to carbon monoxide on oxide-derived nanostructured silver electrocatalysts. *Angew. Chem. Int. Ed.* **55**, 9748–9752 (2016).
- Liu, S. B. et al. Shape-dependent electrocatalytic reduction of CO_2 to CO on triangular silver nanoplates. *J. Am. Chem. Soc.* **139**, 2160–2163 (2017).
- Kim, D. et al. Selective CO_2 electrocatalysis at the pseudocapacitive nanoparticle/ordered-ligand interlayer. *Nat. Energy* **5**, 1032–1042 (2020).
- Moussallem, I., Joerissen, J., Kunz, U., Pinnow, S. & Turek, T. Chlor-alkali electrolysis with oxygen depolarized cathodes: history, present status and future prospects. *J. Appl. Electrochem.* **38**, 1177–1194 (2008).
- Karlsson, R. K. B. & Cornell, A. Selectivity between oxygen and chlorine evolution in the chlor-alkali and chlorate processes. *Chem. Rev.* **116**, 2982–3028 (2016).
- Gupta, N., Gattrell, M. & MacDougall, B. Calculation for the cathode surface concentrations in the electrochemical reduction of CO_2 in KHCO_3 solutions. *J. Appl. Electrochem.* **36**, 161–172 (2006).
- Kim, B., Ma, S., Jhong, H. R. M. & Kenis, P. J. Influence of dilute feed and pH on electrochemical reduction of CO_2 to CO on Ag in a continuous flow electrolyzer. *Electrochim. Acta* **66**, 271–276 (2015).
- Burdyn, T. & Smith, W. A. CO_2 reduction on gas-diffusion electrodes and why catalytic performance must be assessed at commercially-relevant conditions. *Energy Environ. Sci.* **12**, 1442–1453 (2019).
- Li, J. et al. Efficient electrocatalytic CO_2 reduction on a three-phase interface. *Nat. Catal.* **1**, 592–600 (2018).
- Tian, Y., Wang, Z. Y. & Wang, L. Q. Hollow fibers: from fabrication to applications. *Chem. Commun.* **57**, 9166–9177 (2021).
- Rosen, J. et al. Mechanistic insights into the electrochemical reduction of CO_2 to CO on nanostructured Ag surfaces. *ACS Catal.* **5**, 4293–4299 (2015).
- Dunwell, M., Luc, W., Yan, Y., Jiao, F. & Xu, B. Understanding surface-mediated electrochemical reactions: CO_2 reduction and beyond. *ACS Catal.* **8**, 8121–8129 (2018).
- Gu, J., Hsu, C. S., Bai, L., Chen, H. M. & Hu, X. Atomically dispersed Fe^{3+} sites catalyze efficient CO_2 electroreduction to CO. *Science* **364**, 1091–1094 (2019).
- Ma, M., Liu, K., Shen, J., Kas, R. & Smith, W. A. In situ fabrication and reactivation of highly selective and stable Ag catalysts for electrochemical CO_2 conversion. *ACS Energy Lett.* **3**, 1301–1306 (2018).
- Shan, W. Y. et al. In situ surface-enhanced Raman spectroscopic evidence on the origin of selectivity in CO_2 electrocatalytic reduction. *ACS Nano* **14**, 11363–11372 (2020).
- Yan, X. P. et al. Efficient electroreduction of CO_2 to C_{2+} products on CeO_2 modified CuO. *Chem. Sci.* **12**, 6638–6645 (2021).
- Rudolph, W. W., Irmer, G. & Königsberger, E. Speciation studies in aqueous HCO_3^- - CO_3^{2-} solutions. A combined Raman spectroscopic and thermodynamic study. *Dalton Trans.* **7**, 900–908 (2008).
- Chen, X. Y. et al. Electrochemical CO_2 -to-ethylene conversion on polyamine-incorporated Cu electrodes. *Nat. Catal.* **4**, 20–27 (2021).
- An, H. et al. Sub-second time-resolved surface-enhanced Raman spectroscopy reveals dynamic CO intermediates during electrochemical CO_2 reduction on copper. *Angew. Chem. Int. Ed.* **60**, 16576–16584 (2021).
- Iwasita, T., Rodas, A. & Pastor, E. Vibrational spectroscopy of carbonate adsorbed on Pt (111) and Pt (110) single-crystal electrodes. *J. Electroanal. Chem.* **383**, 181–189 (1995).
- Chernyshova, I. V., Somasundaran, P. & Ponnurangam, S. On the origin of the elusive first intermediate of CO_2 electroreduction. *Proc. Nat. Acad. Sci. USA* **115**, E9261–E9270 (2018).
- Moradzaman, M. & Mul, G. In situ Raman study of potential-dependent surface adsorbed carbonate, CO, OH, and C species on Cu electrodes during electrochemical reduction of CO_2 . *ChemElectroChem* **8**, 1478–1485 (2021).

Acknowledgements

This work was financially supported by the National Natural Science Foundation of China (nos. 91745114, 21802160), the “Transformational Technologies for Clean Energy and Demonstration”, Strategic Priority Research Program of the Chinese Academy of Sciences (no. XDA 21000000), the Hundred Talents Program of Chinese Academy of Sciences (no. 2060299), Shanghai Sailing Program (no. 18YF1425700), Shanghai Functional Platform for Innovation Low Carbon Technology, and the Major Project of the Science and Technology department of Inner Mongolia (no. 2021ZD0020).

Author contributions

S.L. and W.C. conceived the research and designed the experiment. S.L., X.D., C.Z., A.C., Y.So. and G.L. conducted the experiment. S.L., W.C., X.D., C.Z., A.C., Y.So. and G.L. analyzed the data. S.L., W.C., X.D., Y.So., G.L., W.W. and Y.Su. discussed and interpreted the results. W.C., W.W. and Y.Su. supervised the project. S.L., W.C. and X.D. wrote the manuscript with input from all authors. All authors revised the manuscript.

Competing interests

The authors declare no competing interests.

Additional information

Supplementary information The online version contains supplementary material available at <https://doi.org/10.1038/s41467-022-30733-6>.

Correspondence and requests for materials should be addressed to Wei Chen, Wei Wei or Yuhan Sun.

Peer review information *Nature Communications* thanks Jingfu Liu and the other, anonymous, reviewers for their contribution to the peer review of this work.

Reprints and permission information is available at <http://www.nature.com/reprints>

Publisher's note Springer Nature remains neutral with regard to jurisdictional claims in published maps and institutional affiliations.



Open Access This article is licensed under a Creative Commons Attribution 4.0 International License, which permits use, sharing, adaptation, distribution and reproduction in any medium or format, as long as you give appropriate credit to the original author(s) and the source, provide a link to the Creative Commons license, and indicate if changes were made. The images or other third party material in this article are included in the article's Creative Commons license, unless indicated otherwise in a credit line to the material. If material is not included in the article's Creative Commons license and your intended use is not permitted by statutory regulation or exceeds the permitted use, you will need to obtain permission directly from the copyright holder. To view a copy of this license, visit <http://creativecommons.org/licenses/by/4.0/>.

© The Author(s) 2022